

High-precision ground state parameters of the two-dimensional spin-1/2 Heisenberg model on the square lattice

Anders W. Sandvik

Department of Physics, Boston University, 590 Commonwealth Avenue, Boston, Massachusetts 02215 and

School of Physical and Mathematical Sciences, Nanyang Technological University, Singapore

(Dated: January 29, 2026)

Motivated by the need for high-precision benchmark results for basic quantum many-body models, several ground state properties of the square-lattice $S = 1/2$ Heisenberg antiferromagnet are computed (the energy, order parameter, spin stiffness, spinwave velocity, long-wavelength susceptibility, and staggered susceptibility) using extensive quantum Monte Carlo simulations with the stochastic series expansion method. Moderately sized lattices are studied at temperatures T sufficiently low to realize the $T \rightarrow 0$ limit, with significantly reduced statistical errors relative to previous works. Results for periodic $L \times L$ lattices with $L \in [6, 96]$ are tabulated versus L and extrapolations to infinite system size are carried out. The relative statistical errors of the finite-size energies are below 10^{-7} . The extrapolated ground state energy density is $e_0 = -0.669441857(7)$, where the number within parentheses is the statistical error (one standard deviation) of the preceding digit. This value represents an improvement in precision of three orders of magnitude over the previously best result. The leading and subleading finite-size corrections to e_0 are in full quantitative agreement with predictions from chiral perturbation theory, thus further supporting the soundness of both the extrapolations and the theory. The extrapolated sublattice magnetization is $m_s = 0.307447(2)$, which agrees well with previous estimates but with a much smaller statistical error. The coefficient of the linear in L^{-1} correction to m_s^2 agrees with the value from chiral perturbation theory and the presence of a factor $\ln^\gamma(L)$ in the second-order correction is also confirmed, with the previously not known value of the exponent being $\gamma = 0.82(4)$. The finite-size corrections to the staggered susceptibility point to logarithmic corrections also in this quantity. To facilitate benchmarking of methods for which periodic boundary conditions are challenging, results for systems with open and cylindrical boundaries are also listed and their spatially inhomogeneous order parameters are analyzed.

I. INTRODUCTION

In light of ongoing efforts to develop better computational methods for strongly interacting quantum many-body systems, accurate benchmark results for key models are called for. While quantum Monte Carlo (QMC) simulations are limited to models for which the sign problem [1–3] can be avoided, these are the only numerically (statistically) exact methods that can reach arbitrarily low temperatures T for large systems in spatial dimensionality higher than one. In particular, with the stochastic series expansion (SSE) QMC method [4–6] with loop updates [7] and related ground-state projection techniques [8], two-dimensional (2D) $S = 1/2$ quantum spin models have been studied in the $T \rightarrow 0$ limit on lattices with linear size L up to hundreds of lattice constants [9, 10] or even larger in some cases [11]. These system sizes far exceed the current limitations of more versatile ground state techniques, such as the density matrix renormalization (DMRG) method [12–14], a variety of methods based on tensor products (TPs) [15–17] (which also can be formulated for infinite lattices, where there are still other convergence issues [18]), and, more recently, neural networks (NNs) [19, 20]. These emerging approaches essentially produce sophisticated variational states, where the number of optimized parameters in principle can be taken sufficiently large to converge to the true ground state. In practice, there are still formidable challenges with the scaling of the computational effort (both mem-

ory and time) with all these methods. The ability to obtain correct results can then be fairly judged only by comparing with exact solutions or QMC simulations of sign-free models, often with the 2D Heisenberg model as a first non-trivial test beyond DMRG accessible one-dimensional systems [21–27].

The primary motivation for the present work is to provide improved QMC benchmark results for the ground state of the standard 2D $S = 1/2$ Heisenberg antiferromagnet, described by the Hamiltonian

$$H = \sum_{\langle ij \rangle} \mathbf{S}_i \cdot \mathbf{S}_j, \quad (1)$$

where the coupling has been set to unity and $\langle ij \rangle$ represents nearest-neighbor spins on the square lattice with $L \times L$ spins and even L . Most of the results will be for periodic boundary conditions but some quantities obtained with open and cylindrical boundaries will also be listed, to facilitate benchmarking of methods for which calculations with periodic boundaries are challenging. In addition to lists of observables versus the lattice size, $L \rightarrow \infty$ extrapolated values will also be presented. Detailed comparisons will be made with finite-size corrections previously predicted using chiral perturbation theory [28, 29] in the case of periodic $L \times L$ lattices. For the other boundary conditions, the spatially inhomogeneous order parameter will be analyzed.

The Heisenberg model has been studied in many past works with a variety of methods and the nature of the

Néel ordered ground state is now well established [30–46]. Over time, the statistical precision achieved in QMC simulations has increased to a level necessary for detailed tests [8, 42–46] of field-theoretical descriptions [28, 29, 36, 47, 48] of the Néel state. However, TN and NN methods are now in some cases reaching lower estimated variational energy errors for periodic lattices (which are difficult to handle with traditional DMRG methods) than the statistical errors of the best published QMC benchmark results [22]. While these methods ultimately target models with interactions beyond the sign-free bipartite Heisenberg exchange, in particular geometrically frustrated systems, it will still be useful to have improved QMC data for the plain 2D Heisenberg model.

A second motivation for improving on previous results is the continued interest in testing universal scaling behaviors related to the breaking of the $SO(3)$ spin-rotation symmetry, e.g., as predicted in great detail by chiral perturbation theory. The finite-size values of the ground state parameters studied here should be polynomials in the inverse system size [28, 29, 47, 48] with coefficients that themselves depend on the infinite-size parameters. In the case of the sublattice magnetization, a logarithmic (log) correction has also been pointed out [47]. The predicted coefficients of both leading and subleading corrections are successfully tested here to significantly higher precision than previously, including the aforementioned log correction for which a previously not known exponent is determined.

The QMC results reported here were obtained with the SSE method at sufficiently low temperatures to realize the $T \rightarrow 0$ limit. The goal is not to reach the largest possible system sizes but to consider small to moderate lattices and reduce the statistical errors significantly with respect to those in Refs. [44] and [8], which have become standard references for the ground state energy and spin correlations of the 2D Heisenberg model. Other quantities computed here include the spin stiffness, the long-wavelength susceptibility, the spinwave velocity, and the staggered susceptibility. These quantities are known to converge slower than the energy in TP and NN methods and are in some cases difficult to calculate. They should nevertheless also be subjected to rigorous benchmarking alongside variational energy estimates.

The largest system size included in the SSE calculations in Ref. [44] was $L = 16$, which is here extended up to $L = 96$. The error reduction in some observables, in particular the energy, is by orders of magnitude for both the finite-size data and $L \rightarrow \infty$ extrapolated values. The extrapolated energy when constraining fits by chiral perturbation theory input (after testing the consistency of those predictions) is $e_0 = -0.669441857(7)$ while the previously best estimate was $e_0 = -0.669437(5)$. In the case of the order parameter, lattice sizes up to $L = 256$ had been previously studied using a ground state projector method in the valence-bond basis [8], with the extrapolated result $m_s = 0.30743(1)$. An identical result was obtained by fitting both finite-size and finite-temperature

QMC results to forms predicted by chiral perturbation theory [45]. Here the new results for $L \leq 96$ are combined with the previous $m_s^2(L)$ results for $L = 128, 192$ and 256 [8] and extrapolated using a fit including the predicted log correction to the L^{-2} term (the leading correction being linear in L^{-1}). This form without any higher-order corrections fits the data for $L \geq 12$ extremely well, perhaps suggesting that there is no L^{-3} correction. All data for $L \geq 6$ can be fitted with an added L^{-5} correction, which leads to the best extrapolated sublattice magnetization, $m_s = 0.307447(2)$; by far the most precise estimate to date.

The rest of the paper is organized as follows: In Sec. II, after defining the relevant physical observables, the ground-state convergence versus the inverse temperature is discussed and tested. Converged results for different system sizes are tabulated. The observables are extrapolated to the thermodynamic limit in Sec. III and the validity of the forms of the finite-size corrections predicted by chiral perturbation theory is tested. Results for lattices with open and cylindrical boundary conditions are listed in Sec. IV and the edge distortion of the order parameter is also analyzed. Sec. V concludes with a brief summary and discussion.

II. FINITE-SIZE RESULTS

The ground state properties considered here were computed within the efficient SSE operator-loop approach [4, 6], where the partition function is expressed as

$$Z = \sum_{n=0}^{\infty} \frac{(-\beta)^n}{n!} \text{Tr}\{e^{-\beta H}\}, \quad (2)$$

at inverse temperature β . Details of the method and estimators of various observables are described in detail in the existing literature [6, 44], and neither algorithms nor technical implementations will be significantly discussed here. The SSE method itself is formally exact and the results are only affected by standard statistical sampling errors, characterized in the results to be presented here as one standard deviation of the mean. To obtain the ground state parameters of interest, the limit $T \rightarrow 0$ also must be carefully taken. Definitions of the physical observables will be given first in Sec. II A, followed by $T \rightarrow 0$ convergence checks in Sec. II B and finite-lattice results in Sec. II C.

A. Definitions

The internal energy density is obtained in SSE simulations as the mean of the expansion power n in Eq. (2),

$$e = \frac{\langle H \rangle}{N} = \frac{\langle n \rangle}{\beta N}, \quad (3)$$

where $N = L^2$ is the system volume. Not being explicitly dependent on the evolved spin configurations, this is manifestly a spin-rotationally averaged estimator [44]. The width of the distribution of n scales as $\langle n \rangle^{1/2}$ for $T \rightarrow 0$, which together with the above SSE form of e implies that even a single instance of n gives an energy estimate that is good to within an error of order only $(\beta N)^{-1/2}$. For M independent sampled SSE configurations, the statistical error is therefore of order $(\beta NM)^{-1/2}$, i.e., for increasing β and N less sampling is required to achieve a specific statistical precision. For desired precision (standard deviation of the mean) ϵ , the number of independent measurements must be of order $(\epsilon^2 \beta N)^{-1}$. Assuming no N and β dependence of the autocorrelation time of n , the computational effort for generating an independent sample of n scales as βN (in terms of the number of operations performed, disregarding computer technical aspects such as worse cache memory performance for increasing system size), thus, the effort to achieve a desired precision of e would be independent of β and N . The SSE autocorrelation time of n is indeed short and shows almost no dependence on β and N , and the above scaling behavior of e seems to be satisfied in practice. The other size-normalized quantities listed below typically exhibit increasing autocorrelation times with N , and in some cases with β , which is reflected in increasing relative statistical errors with L in the results to be presented below. The total lengths of the SSE simulation runs were adapted to achieve a relative error in $e(L)$ of roughly 10^{-7} for each system size considered.

The following is just a concise list of the other quantities considered, with only minimal comments on how they are estimated within the SSE method. For further technical details, see Refs. [44] and [6].

The order parameter density is the staggered magnetization, which can be taken as a diagonal operator in the SSE simulations,

$$m_s^z = \frac{1}{N} \sum_{i=1}^N (-1)^{x_i+y_i} S_i^z, \quad (4)$$

where (x_i, y_i) are the integer lattice coordinates. The corresponding extensive quantity lacking the N^{-1} factor will also be referred to below; $M_s^z = N m_s^z$. The definition,

$$m_s^2 \equiv 3\langle (m_s^z)^2 \rangle, \quad (5)$$

includes a factor 3 to account for spin-rotational averaging, so that the full symmetry-broken value is obtained in the thermodynamic limit. The expectation value was computed with an efficient loop estimator [6, 7, 42], which, however, was not fully averaged over imaginary time in order to reduce the computational effort of these measurements—given that one of the main aims here is the obtain high-precision results for the energy, the estimator of which demands no computational effort.

The corresponding staggered susceptibility is given by the Kubo integral

$$\chi_s = \frac{1}{N} \int_0^\beta d\tau \langle M_s^z(\tau) M_s^z(0) \rangle, \quad (6)$$

where $M_s^z(\tau)$ is the imaginary-time evolved total sublattice magnetization. This space-time integrated correlator can also in principle be computed with a loop estimator [43] but here a different approach was taken, where an exact expression for the integral is evaluated exactly for each SSE configuration [6, 49] but is not expressed using loop sizes. Though the loop estimator should in principle be more efficient, the results obtained here are still of high statistical quality.

The staggered magnetization corresponds to wavenumber $\mathbf{q} = (\pi, \pi)$ and Eq. (6) generalizes to arbitrary \mathbf{q} :

$$\chi(\mathbf{q}) = \frac{1}{N} \int_0^\beta d\tau \langle M^z(-\mathbf{q}, \tau) M^z(\mathbf{q}, 0) \rangle, \quad (7)$$

where $M^z(-\mathbf{q}, \tau)$ is the Fourier transform of the spins at fixed imaginary time (here not normalized by N),

$$M^z(\mathbf{q}, \tau) = \sum_{i=1}^N e^{-\mathbf{r}_i \cdot \mathbf{q}} S_i^z, \quad (8)$$

with $\mathbf{r}_i = (x_i, y_i)$. For $q = 0$, $M_{\mathbf{q}}^z$ is the conserved uniform magnetization and the Kubo integral then reduces to the classical form of the uniform susceptibility

$$\chi_u = \frac{1}{NT} \left(\sum_{i=1}^N S_i^z \right)^2, \quad (9)$$

which vanishes identically in the singlet ground state. The long-wavelength susceptibility is considered here by using $\mathbf{q}_1 = (2\pi/L, 0)$ or $\mathbf{q}_1 = (0, 2\pi/L)$ in Eq. (7). In the gapless symmetry broken state, the transverse component χ_{\perp} of this susceptibility is a key ground state parameter, which can be obtained in the large- L limit from $\chi(q_1)$ by including a rotational factor $3/2$ (reflecting the fact that the longitudinal component should vanish as $T \rightarrow 0$ on account of the conserved magnetization and gapped longitudinal fluctuations). We thus define

$$\chi_{\perp} = \frac{3}{2} \chi(q_1). \quad (10)$$

The spin stiffness for systems defined on periodic lattices is computed using the total spin current (winding number) fluctuations [44, 50] as

$$\rho_s = \frac{3}{4\beta N} \langle W_x^2 + W_y^2 \rangle, \quad (11)$$

where W_a , $a \in \{x, y\}$, is the current along the a lattice direction integrated over imaginary time (which is done exactly with the SSE estimator),

$$W_a = \int_0^\beta d\tau J_a(\tau), \quad (12)$$

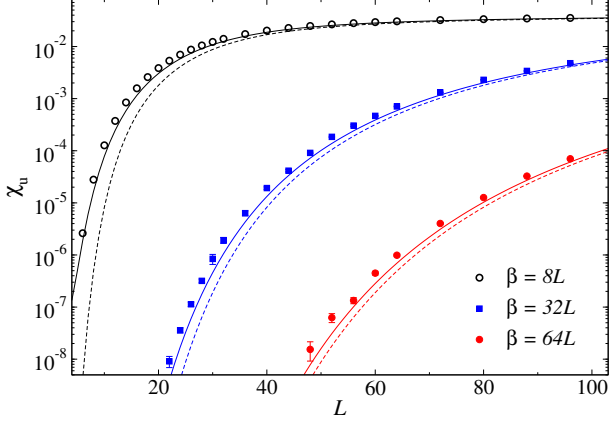


FIG. 1. Uniform susceptibility versus the system size for three values of the aspect ratio β/L . The dashed lines show predictions based on a quantum rotor tower with the infinite-size value of the $T = 0$ susceptibility, $\chi_u(\infty) = 0.04379$, while the solid lines show results for $\chi_u(L)$ given by a fourth-order polynomial fitted to the finite-size data in Table I.

which is an integer multiple (the winding number) of the system length L in a periodic system. Eq. (11) also contains a factor $3/2$ to account for the difference between rotationally invariant finite systems and the symmetry-broken state in the thermodynamic limit.

The spinwave velocity can be obtained from the stiffness and the transverse susceptibility using a formula originating from the hydrodynamic description [31] of the long-wavelength fluctuations of the Néel state,

$$c = \sqrt{\frac{\rho_s}{\chi_\perp}}, \quad (13)$$

which should be exact when the $L \rightarrow \infty$ limit is taken of ρ_s and $\chi(q_1)$. Finite-size results $c(L)$ based on the same formula will also be presented here.

B. Finite-temperature effects and $T \rightarrow 0$ convergence

In order to judge remaining effects of finite temperature in the SSE simulations, the tower of Anderson quantum rotor excitations [30] can be analyzed. For the 2D system, these excitations with total spin $S > 0$ (the ground state having $S = 0$) should have the exact asymptotic form

$$E(S) = \frac{S(S+1)}{2\chi_\perp L^2} \quad (14)$$

for S up to order $L^{1/2}$ and large L (and with $L^2 \rightarrow L^d$ for a d -dimensional system). These rotor states fall below the lowest spinwave excitation (the energy of which is of order L^{-1}) and become degenerate with the ground state as $L \rightarrow \infty$, thus allowing for the spontaneous breaking of the $\text{SO}(3)$ symmetry of the Néel order parameter. A

pedagogical derivation of the numerator in Eq. (14) can be found in Ref. [6].

The L^{-2} scaling of the rotor excitations immediately implies that full convergence to the ground state requires the inverse temperature to grow with L as $\beta \propto L^2$. In practice, convergence can be tested by monitoring computed expectation values versus β . It is then useful to pay particular attention to quantities that are expected to converge slowly, e.g., the staggered susceptibility Eq. (6), where the integral over τ is of a very slowly decaying correlator and β has to be large not only to converge equal-time properties but also to accommodate sufficiently large τ for the correlations to vanish exponentially, ultimately as $e^{-E(S)\tau}$ with $S = 1$ in Eq. (14).

Another useful quantity is the uniform susceptibility Eq. (9), which vanishes identically in the singlet ground state but is non-zero at any $T > 0$, ultimately on account of the $S > 0$ rotor states at very low T . Fig. 1 shows the susceptibility versus the system size when β is scaled only linearly with L as $\beta = aL$, but with rather large factors $a = 8, 32$, and 64 . The results are compared with the prediction from the rotor spectrum Eq. (14);

$$\chi_u(T) = \frac{1}{Z} \sum_{S=1}^L e^{-E(S)/T} \sum_{m=-S}^S m^2, \quad (15)$$

where the partition function is

$$Z = 1 + \sum_S (2S+1) e^{-E(S)/T}. \quad (16)$$

Here the upper bound for S should be of order $L^{1/2}$, reflecting the scale at which the rotor energy is comparable to the lowest spinwave energy. However, at the low temperatures of interest here the expectation value is completely dominated by $S \ll L$ and the exact value of the cutoff is not important (it is taken all the way to $S = L$ in the calculations here). The value of the perpendicular susceptibility in Eq. (14) is here taken from the infinite-size polynomial extrapolation (discussed in Sec. III) of the data in Table I, which results in the dashed curves in Fig. 1. Though there are clearly deviations, the predictions approach the SSE results as L increases. To account for some of the finite-size corrections, χ_\perp can alternatively be treated as a size dependent quantity $\chi_\perp(L)$, which can be evaluated for arbitrary L using the same fitted polynomial as used for the $L \rightarrow \infty$ extrapolation. As shown with the solid curves in Fig. 1, the deviations when using $\chi_\perp(L)$ are even smaller and leave little doubt that the rotor tower provides a good (asymptotically exact) description for temperatures below the lowest spinwave excitations. The deviations in Fig. 1 from the predicted curves can be explained by finite-size corrections to the rotor spectrum. These corrections have been studied in previous works [5, 6, 51, 52].

From the partition function Eq. (16) we can also compute the probability P_0 of the system being in the ground state. Given that the weight of the ground state is 1

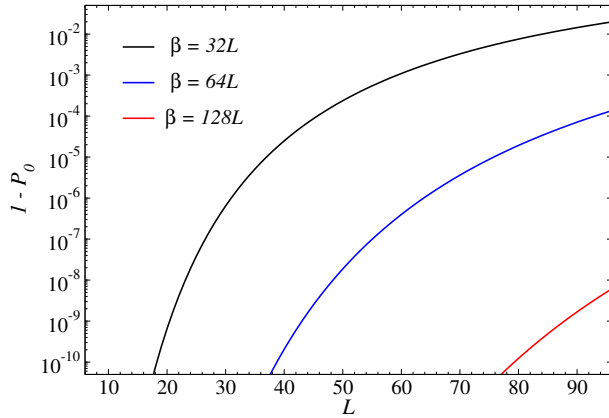


FIG. 2. Probability vs the lattice size of the system being thermally excited (P_0 being the ground-state probability) under the valid assumption that only the rotor states contribute. The results for $\beta = 32$ (black), 64 (blue) and 128 (red) were computed using the interpolated $\chi_{\perp}(L)$ function in the rotor spectrum Eq. (14), the same as used for the solid curves in Fig. 1. The range of $L \in [6, 96]$ corresponds to that for which SSE results are presented here.

in Eq. (16), we simply have $P_0 = Z^{-1}$. The corresponding probability $1 - P_0$ of the system being excited into the rotor tower is graphed versus the system size at $\beta/L = 32, 64$, and 128 in Fig. 2. Convergence of computed observables were confirmed explicitly by comparing results at different β values, but the results in Fig. 2 are also useful for judging whether results of the two different calculations can be averaged and still effectively maintain the $T = 0$ limit. Most physical observables change very little, in a relative sense, between the ground state and a low-lying excited state, e.g., the energy density of a rotor state is only of order N^{-2} above the ground state. Therefore, the relative finite-temperature corrections in such observables will be orders of magnitude smaller than the excitation probabilities in Fig. 2.

It should be noted here that simulations with β larger than what is strictly needed to obtain $T \rightarrow 0$ results is not a waste of computer resources, because the amount of statistical data contained in the SSE configurations scales linearly with β , i.e., in the same way as the nominal computational effort of the simulations—the example of the energy was already discussed explicitly at the beginning of Sec. II. An excessively large β can still be detrimental in practice because of memory limitations and poor cache performance. The calculations reported here were mostly limited to $\beta/L \leq 64$ and system sizes $L \leq 96$, with some limited test results generated also at $\beta/L = 128$ for $L = 80, 88$, and 96.

In this work the $T \rightarrow 0$ limit is effectively taken first for each system size L , with results presented below in Sec. II C. Such ground state data will be useful for benchmarking other methods, as discussed in Sec. I. The $L \rightarrow \infty$ limit of the various observables will be considered in Sec. III by fitting the finite- L data sets to polynomials

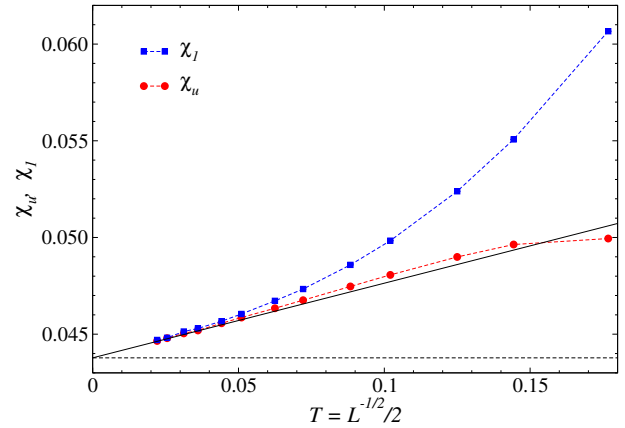


FIG. 3. Temperature dependent $q \rightarrow 0$ susceptibility computed in two different ways in simulations with $\beta = 2L^{1/2}$; with $q = 0$ in χ_u and $q = 2\pi/L$ in χ_1 . The dashed line is the $T = 0$ value obtained by extrapolating the χ_{\perp} data in Table I to the thermodynamic limit and adjusted for the factor 3/2 in Eq. (7). The black solid line is a linear fit to the χ_u data. The other dashed lines are guides to the eye.

in L^{-1} —the predicted form of the finite-size corrections (in one case with a log correction) [28, 29, 47] that will be tested as one of the aims of this work.

It is worth pointing out that the limits $L \rightarrow \infty$ and $T \rightarrow 0$ can be taken in either order for most quantities that do not diverge when $T \rightarrow 0$. A prominent exception is the uniform susceptibility, Eq. (9), on account of the vanishing conserved magnetization as $T \rightarrow 0$ for any L . However, the uniform magnetization can also be taken as the limit $q \rightarrow 0^+$, in practice with $q_1 = 2\pi/L$, of the general susceptibility in Eq. (7), which does not vanish when $T \rightarrow 0$ for any L . The limit can then safely be taken with $T \rightarrow 0$ data versus L .

Though we will here not use alternative approaches to taking the limit $L \rightarrow \infty$ first and then $T \rightarrow 0$, it is interesting to note that the two limits can also in principle be taken simultaneously as a function of a single parameter, by considering a size dependent temperature $T(L)$, adapted such that a sufficient fraction of the quantum rotor states fall below this temperature. A natural choice in terms of the inverse temperature is $\beta = aL^{1/2}$, with a an essentially arbitrary constant (with value only relevant as far as it determines the rate of convergence to the $T \rightarrow 0$ limit). Fig. 3 shows results versus the temperature for both χ_u and $\chi_1 = \chi(q_1)$ obtained with $\beta = 2L^{1/2}$. Here the equality of the two susceptibilities in the limit $T \rightarrow 0$ can be observed clearly.

C. Tabulated numerical data

All the computed finite-size data for the quantities defined in Sec. II A are listed in Table I. The length of the SSE runs generating these results were adapted to achieve a statistical error less than 3×10^{-8} in the en-

TABLE I. Results for different system sizes computed at inverse temperature $\beta/L = 64$ for $L > 48$ and averaged over $\beta/L = 32$ and $\beta/L = 64$ simulations for $L \leq 48$. The digits within parentheses indicate the statistical error (one standard deviation rounded to a single digit) of the preceding digit of the mean.

L	e_0	ρ_s	χ_{\perp}	c	m_s^2	χ_s/L^2
6	-0.67887215(2)	0.2375897(1)	0.0936076(1)	1.593155(1)	0.2098368(2)	0.01324669(3)
8	-0.67349005(2)	0.2205407(1)	0.0854012(1)	1.606987(1)	0.1778419(2)	0.01038140(3)
10	-0.67155266(2)	0.2112378(1)	0.0806085(2)	1.618809(2)	0.1593710(2)	0.00883242(4)
12	-0.67068192(2)	0.2054239(1)	0.0775450(2)	1.627604(2)	0.1474495(3)	0.00788157(4)
14	-0.67023225(2)	0.2014610(2)	0.0754479(3)	1.634075(3)	0.1391544(4)	0.00724419(5)
16	-0.66997660(2)	0.1985904(2)	0.0739352(3)	1.638904(4)	0.1330657(4)	0.00678935(6)
18	-0.66982043(2)	0.1964164(3)	0.0728004(4)	1.642562(5)	0.1284152(5)	0.00644930(7)
20	-0.66971967(2)	0.1947161(3)	0.0719222(5)	1.645393(5)	0.1247499(6)	0.00618556(7)
22	-0.66965176(2)	0.1933480(4)	0.0712254(5)	1.647603(7)	0.1217905(7)	0.00597567(9)
24	-0.66960434(2)	0.1922247(4)	0.0706606(6)	1.649361(7)	0.1193517(7)	0.00580444(9)
26	-0.66957017(3)	0.1912848(6)	0.0701934(8)	1.65079(1)	0.1173082(9)	0.0056624(1)
28	-0.66954496(3)	0.1904871(7)	0.0698049(9)	1.65192(2)	0.115573(1)	0.0055424(1)
30	-0.66952595(3)	0.1898036(8)	0.069472(1)	1.65290(2)	0.114080(1)	0.0054402(2)
32	-0.66951133(3)	0.1892070(9)	0.069188(1)	1.65368(2)	0.112781(1)	0.0053516(2)
36	-0.66949091(3)	0.188225(1)	0.068725(1)	1.65493(2)	0.110638(2)	0.0052065(2)
40	-0.66947775(3)	0.187448(2)	0.068368(2)	1.65583(2)	0.108941(2)	0.0050922(2)
44	-0.66946890(3)	0.186819(2)	0.068083(2)	1.65650(2)	0.107570(2)	0.0050002(3)
48	-0.66946275(3)	0.186297(2)	0.067855(2)	1.65696(3)	0.106426(2)	0.0049241(3)
52	-0.66945833(3)	0.185860(2)	0.067661(2)	1.65738(3)	0.105475(2)	0.0048610(3)
56	-0.66945502(3)	0.185483(2)	0.067501(2)	1.65766(3)	0.104660(3)	0.0048065(3)
60	-0.66945260(3)	0.185158(3)	0.067367(3)	1.65786(4)	0.103955(3)	0.0047601(4)
64	-0.66945072(3)	0.184876(3)	0.067244(3)	1.65811(4)	0.103342(3)	0.0047196(4)
72	-0.66944815(3)	0.184411(4)	0.067051(4)	1.65841(5)	0.102330(4)	0.0046527(5)
80	-0.66944645(3)	0.184039(5)	0.066905(4)	1.65853(6)	0.101528(4)	0.0046001(5)
88	-0.66944530(3)	0.183736(6)	0.066775(5)	1.65879(7)	0.100864(5)	0.0045555(6)
96	-0.66944454(3)	0.183481(7)	0.066674(6)	1.65889(8)	0.100334(6)	0.0045176(7)

ergy (rounded to one digit in the table). The other quantities have larger errors. In some cases similar errors were achieved in previous studies, e.g., in Ref. [8] the staggered magnetization was computed using a valence-bond projector QMC method for sizes up to $L = 256$, with errors only somewhat exceeding those in Table I for the larger common system sizes. The results of the two calculations agree perfectly within statistical errors. None of the quantities in Table I have previously been available at the level of statistical precision achieved here. They will hopefully be useful for benchmarking beyond just the energy.

The results for $L \leq 30$ represent averages over simulations at $\beta/L = 32$ and 64. The averaging is validated by the fact that the results agree to within statistical errors as well as the behaviors of the excitation probabilities graphed in Fig. 2. There is good statistical agreement between most of the data at the two β values also for the larger systems, with the exception of staggered susceptibility χ_s , which will be further discussed below. The good agreement for all other quantities serves as a vali-

dation of the $\beta/L = 64$ data being fully converged within the error bars.

In the case of χ_s , results at $\beta/L = 32$ and 64 agree within statistical errors only for $L \leq 60$. For larger systems the differences are still minor, e.g., for the largest system (and deviation) $L = 96$ the $\beta/L = 64$ value is about 2% larger. Given this small difference, the asymptotically expected exponential convergence with β , and the size dependence of the ground state probabilities in Fig. 2, the $\beta/L = 64$ values should be fully converged within statistical errors for all $L < 80$. Limited results (with somewhat lower statistical precision) at $\beta/L = 128$ for $L = 80, 88$, and 96 also confirm close convergence, with the remaining finite- T deviation for $L = 96$ estimated to be at most 1-2 standard deviations and insignificant for $L = 80$ and 88.

For $L = 6$, the ground state energy to nine significant digits is $e_0 = 0.678872150$ from Lanczos exact diagonalization and the staggered magnetization squared is $m_s^2 = 0.209837151$. The corresponding results in Table I are statistically fully consistent with these values, thus

demonstrating the unbiased nature of the SSE method. For $L = 10$, a very precise SSE result was recently obtained, $e_0 = -0.67155267(5)$ [22], where the relative error as small as 10^{-7} was needed in order to test an even more precise variational NN results; $e_0 = -0.67155260(3)$. These results also agree perfectly with the $L = 10$ energy in Table I, where the statistical error is even smaller.

Recently an approach based on recurrent NNs was used to compute energies for L up to 32, with claimed errors in the seventh decimal place [27]. In principle this method should be variational, but the reported energies extrapolated to zero variance are in some cases below the values in Table I, including the $L = 10$ system for which the earlier high-precision NN result quoted above agrees with the present SSE result. The discrepancy demonstrates the difficulties associated with variance extrapolations, though it is still impressive that the results are good to five decimal places.

III. FINITE-SIZE CORRECTIONS AND INFINITE-SIZE EXTRAPOLATIONS

The form of the finite-size scaling corrections in ordered antiferromagnets have been derived within spin-wave theory [34] as well as more sophisticated symmetry based approached [47, 48], in the most refined form to high orders in chiral perturbation theory [28, 29]. The general form of all the quantities that will be considered here is a polynomial in the inverse system size, with some of the low-order coefficients given explicitly in terms of infinite-size ground-state parameters. Because of the high statistical precision of the data, higher-order terms also have to be included in order to obtain good fits when the smaller system sizes are included.

Some of the predicted low-order coefficients were tested in Ref. [44] with data for system sizes only up to $L = 16$. Despite the now modest lattices, agreement was found to within a few percent for the leading corrections in independent polynomial fits. A collective fit to several quantities, constrained by the predicted forms, gave statistically more precise values of the coefficients. In some cases, in particular the spin stiffness and velocity, the extrapolated values deviate somewhat (by several error bars) from later determined values, e.g., in Refs. [45, 46]. In hindsight, the system sizes $L \leq 16$ in Ref. [44] were too small to completely avoid distorting effects of corrections of higher order than those included. No such bias has been claimed in the case of the energy, however.

With the much reduced statistical errors and larger range of system sizes, the predicted $T = 0$ finite-size corrections can now be tested more precisely. The three predicted forms that will be considered here are for the energy, the sublattice magnetization, and the staggered

susceptibility [28, 29, 47]:

$$e_0(L) = e_0 - \frac{Ac}{L^3} + \frac{1}{4\chi_\perp} \frac{1}{L^4} + \dots, \quad (17a)$$

$$m_s^2(L) = m_s^2 + \frac{Bm_s^2}{\sqrt{\rho_s\chi_\perp}} \frac{1}{L} + \frac{\mu \ln^\gamma(L/\xi)}{L^2} + \dots, \quad (17b)$$

$$\frac{\chi_s(L)}{L^2} = m_s^2 \left(\frac{2\chi_\perp}{3} + \frac{C}{c} \frac{1}{L} + \frac{C}{\rho_2} \frac{1}{L^2} \right) + \dots, \quad (17c)$$

where the symbols without (L) refer to the infinite-size values and the constants A , B , and C are

$$A = 1.437745, \quad B = 0.6207465, \quad C = 0.1918021. \quad (18)$$

Note that the second-order term in Eq. (17b) includes a multiplicative log correction with unknown prefactor μ and exponent γ [47]. No logs have been claimed in the other quantities. Note also that the leading correction to the energy is of order L^{-3} and the factor of the L^{-4} correction also has a definite predicted value in terms of only the transverse susceptibility [28]. The second-order correction to χ_s was obtained in Ref. [29]. In the original literature on the finite-size corrections, many of the coefficients in Eqs. (17) were expressed using the spinwave velocity c . Here, by using Eq. (13) c has been eliminated in some of the terms for simplified expressions.

Though in principle combined fits to several quantities can be employed [42, 44, 45], here independent fits of all the quantities will be carried out first. A small number of terms (typically two) beyond those included in Eqs. (17) will be added in order to capture remaining finite-size corrections for the still relatively small system sizes available here. The consistency of those coefficients that are predicted in Eqs. (17) can then be tested with the extrapolated $L \rightarrow \infty$ quantities (i.e., the zeroth-order coefficients). Satisfactory agreement between the fitted and predicted coefficients then not only supports the theoretical underpinnings of Eqs. (17) but can also be taken as confirmation the soundness of the extrapolations; specifically the lack of impact of neglected terms of higher order than the corrections included. Having established confidence in the forms Eqs. (17), the precision of the extrapolated e_0 and m_s will be further improved by statistical imposition of the values of χ_\perp and ρ_s in their leading corrections. In all fits below, the raw data without truncating at the level of the one-digit statistical error (in Table I) were used for full statistical soundness of the procedures.

A. Uniform susceptibility, spin stiffness, and spinwave velocity

In order to eventually test and use Eqs. (17), we begin by extrapolating $\rho_s(L)$ and $\chi_\perp(L)$ in Table I, using unconstrained polynomials of fourth order. Marginally good fits are then obtained when including system sizes $L \geq 10$ for ρ_s and $L \geq 8$ for χ_\perp . Increasing the

minimum size L_{\min} included in the fits to $L_{\min} = 12$ and $L_{\min} = 10$, respectively, leads to fully satisfactory goodness-of-fit per degree of freedom; $\chi^2/N_{\text{dof}} \approx 1.1$ (for ρ_s) and 0.89 (for χ_{\perp}). The $L \rightarrow \infty$ extrapolated values (constants in the fits) are then $\rho_s = 0.180752(6)$ and $\chi_{\perp} = 0.065690(5)$. The result from constrained fits to $L \leq 16$ data in Ref. [44] were $\rho_s = 0.175(2)$ and $\chi_{\perp} = 0.0625(9)$, both smaller than the present estimates by about three of their error bars, reflecting some effects of corrections beyond the only quadratic fits used there. A later SSE result obtained from the quantum rotor states of large systems by analyzing the effects of an external magnetic field on the uniform magnetization gave $\chi_{\perp} = 0.0659(2)$ [5], which is consistent with the present result but with much larger error. In Ref. [45] $\rho_s = 0.18081(11)$ was obtained, likewise consistent with the present result within its ten times larger error.

The spinwave velocity c is also an important ground state parameter and appears in both Eq. (17a) and Eq. (17c). Extrapolating the finite-size results for c in Table I with $L_{\min} = 12$ gives $c = 1.65881(7)$ ($\chi^2/N_{\text{dof}} \approx 1.1$). Its value according to Eq. (13) with the above ρ_s and χ_{\perp} values is consistent with the same value but with a marginally smaller error bar; $c = 1.65880(6)$, which will be used below. This value is statistically less precise than and inconsistent with (deviating by about five error bars from) an indirectly computed value $c = 1.65847(4)$ [46] obtained with SSE simulations at different aspect ratios L/β and locating the special ratio $(L/\beta)^*$ at which the spatial and temporal winding number fluctuations are equal. At that point the system is effectively space-time symmetric and $c = (L/\beta)^*$. This method had previously been used with less precise data in Ref. [45], with the result $c = 1.6586(3)$. Given the overall trends of $c(L)$ in Table I, it is unlikely that the value could be as low as $c = 1.65847(4)$ obtained in Ref. [46]. Determining the cubic ratio $(\beta/L)^*$ is also more involved [46] than the simple fitting of simple SSE estimators used here, thus having higher risks of underestimating the errors propagating from all steps. The value and error bar obtained by the simple extrapolations above are therefore likely more reliable

B. Ground state energy

We now proceed to test the form Eq. (17a) of the ground state energy. The approach taken here is again to use a polynomial of high enough order to obtain a statistically sound fit even when small system sizes are included. Adding terms of order L^{-5} and L^{-6} in Eq. (17a), i.e., with five adjustable parameters in total, a fit to all the data for $L \geq 6$ from Table I has excellent goodness-of-fit, $\chi^2/N_{\text{dof}} = 0.94$. However, the predicted L^{-3} and L^{-4} coefficients in Eq. (17a) are not perfectly reproduced. Denoting these coefficients by e_3 and e_4 , respectively, the ρ_s and χ_{\perp} values determined above correspond to $e_3 = 2.38493(8)$ and $e_4 = 3.8058(3)$, while the fit with

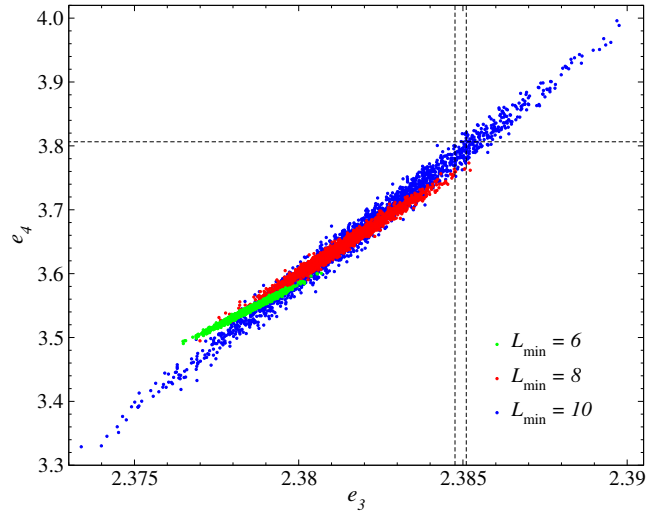


FIG. 4. Scatter plot of the coefficients of the cubic and quartic corrections of the energy based on 2000 fits with Gaussian noise added to the energy data in Table I, with the minimum size being $L_{\min} = 6$ (green dots), 8 (red dots), and 10 (blue dots). The horizontal and vertical pairs of dashed lines indicate the expected values based on Eq. (17) with ρ_s and χ_{\perp} taking the previously extrapolated values, plus and minus two standard deviations in each case. The two horizontal lines almost coincide on the scale used here.

minimum size $L_{\min} = 6$ produces $e_3 = 2.3785(6)$ and $e_4 = 3.54(2)$. Increasing the minimum size to $L_{\min} = 8$ gives $e_3 = 2.383(2)$, which is consistent with the predicted value, while $e_4 = 3.64(5)$ is only marginally consistent, deviating by about three error bars. Increasing the minimum size to $L_{\min} = 10$, both parameters are fully consistent with the predicted values but the error bars of course are larger as well; $e_3 = 2.382(3)$ and $e_4 = 3.7(1)$

The fitted coefficients are not statistically independent, and for a view of their correlated statistical fluctuations it is useful to examine the full distribution $P(e_3, e_4)$. Here this distribution is generated by adding Gaussian noise to the energy data in Table I, with mean zero and standard deviation equal to the one-standard deviation statistical errors. Results based on 2000 fits with different noise realizations are shown in Fig. 4 for $L_{\min} = 6, 8$, and 10. The predicted values of the coefficients are indicated by the vertical and horizontal lines. It is obvious that the fitted coefficients (e_3, e_4) indeed are highly correlated and that the $L_{\min} = 6$ fits do not produce valid coefficients. The agreement is better with $L_{\min} = 8$, though still not acceptable, with the part of the distribution with significant probability density still slightly outside the box corresponding to the jointly allowed values. Only with $L_{\min} = 10$ do the fits produce a distribution with statistically plausible overlap with the box, and for $L_{\min} = 12$ (not shown) the box is well inside the (still larger) high-probability region. The individually computed values with statistical errors quoted above correspond to projecting the two-dimensional distribution onto the e_3 and

e_4 axes. These distributions are much broader than the thickness of the very elongated full distributions. Fig. 4 shows that the agreement with both of the the predicted values for $L_{\min} = 10$ is actually much better than indicated by just the independent error bars, in the sense that fixing one of the coefficients to within its predicted window gives a very small error bar of the second coefficient, and that coefficient is then also consistent with the prediction.

The extrapolated $L \rightarrow \infty$ energy for $L_{\min} = 10$ is $e_0 = -0.669441865(11)$ and the results for $L_{\min} = 8$ and $L_{\min} = 6$ are also fully consistent with this value, $e_0 = -0.669441866(10)$ and $e_0 = -0.669441878(9)$, respectively. These results are also statistically fully consistent with the often quoted previously best infinite-size value [44], $e_0 = -0.669437(5)$, where the error is about 500 times larger. Given the almost identical results for $L_{\min} = 8$ and $L_{\min} = 10$, the final result of this analysis is taken as $e_0 = -0.669441866(10)$.

Given that there should now be no doubt about the applicability of Eq. (17a) in combination with the higher-order corrections, an even more precise extrapolated energy can be obtained by constraining the fit by imposing the values of the coefficients e_3 and e_4 within their statistical errors. As an alternative to carrying out such a constrained fit, an equivalent method is to use the distribution $P(e_3, e_4)$ and compute the mean energy from only those fits that produce e_3 and e_4 values falling within the box marking the allowed statistically acceptable window (of size one standard deviation in each direction). Sampling millions of points, for $L_{\min} = 10$ only about $8 \times 10^{-3}\%$ of them satisfy the constraints (reflecting the small size of the allowed box inside the much larger region of significant weight in the sampled distribution) and the mean goodness-of-fit of the points satisfying the constraint is good, with $\langle \chi^2 \rangle / N_{\text{dof}} < 1$ (after correcting for the fact that there are two sources of fluctuations when Gaussian noise is added to data already affected by the statistical errors in the SSE simulations). The mean energy with $L_{\min} = 10$ is $e_0 = -0.669441861(6)$, while increasing to $L_{\min} = 12$ changes the result only very little, to $e_0 = -0.669441857(7)$, with $6 \times 10^{-3}\%$ of the points satisfying the constraints.

Since, it may be argued, the $L_{\min} = 10$ distribution in Fig. 4 is not fully satisfactory in relation to the predicted allowed window of (e_3, e_4) , while for $L_{\min} = 12$ (where the not shown distribution covers a larger area) the allowed window is in a region of high probability density, the $L_{\min} = 12$ value $e_0 = -0.669441857(7)$ is here presented as the final result for the ground state energy; the relative statistical error here is unprecedented at 10^{-8} and no systematic errors should be expected. Note that the value is only about one error bar smaller than in the plain extrapolated $L_{\min} = 10$ and $L_{\min} = 12$ results; thus there is full statistical consistency but the error bar with the constraint imposed is about 30% smaller.

C. Staggered magnetization

When fitting data for the staggered magnetization, the results for larger system sizes from Ref. [8] will also be included. These are

$$\begin{aligned} m_s^s(L = 128) &= 0.098843(16), \\ m_s^s(L = 192) &= 0.097371(11), \\ m_s^s(L = 256) &= 0.096669(17). \end{aligned} \quad (19)$$

In addition to marginally improving the final estimate of m_s , these values from a different calculation also serves as an independent consistency test. The two best previous estimates of the $L \rightarrow \infty$ order parameter are both $m_s = 0.30743(1)$ [8, 45]. The result in Ref. [8] was obtained by extrapolating the long-distance ($r = L/2$) spin correlation function, which has less size dependence than the space-integrated correlator m_s^2 . In Ref. [45], a collective fit to temperature and size dependent data was used with constraints from chiral perturbation theory.

Before considering the predicted log correction of the quadratic term in Eq. (17b), it is interesting to explore purely polynomial fits to $m_s^2(L)$. The log correction was included previously in Ref. [40] (though with data from a biased QMC method) but not in Refs. [44] and [8]. A fourth-order polynomial fits well the $L \leq 12$ data ($\chi^2 / N_{\text{dof}} \approx 1.1$, while for $L_{\min} = 10$ the value is slightly too high at $\chi^2 / N_{\text{dof}} \approx 1.9$) and gives $m_s = 0.30739(1)$. This result is only marginally consistent with the previous estimates and has a similar error bar; with two significant digits in the error the result is $m_s = 0.307387(10)$. Reducing the order of the polynomial to third order, a good fit can only be obtained when the minimum size is increased to $L_{\min} = 20$ ($\chi^2 / N_{\text{dof}} \approx 1.0$), reflecting the sensitivity of the fit to the high-order corrections that are manifested in the small-size data with very small error bars. The result is then $m_s = 0.307394(12)$, fully consistent with the fourth-order result and marginally consistent with the previous best results.

Returning to the fourth-order fit with $L_{\min} = 12$, even though χ^2 / N_{dof} is good the first-order coefficient $m_1 = 0.5463(6)$, is rather far from the predicted value $m_1 = B m_s^2 (\rho_s \chi_{\perp})^{-1/2} = 0.53826(4)$ when the constant m_s^2 from the fit is used along with the previously determined ρ_s and χ_{\perp} values. The agreement is also not improved if the minimum size $L_{\min} = 14$ is used, which still gives an excessively large coefficient $m_1 = 0.5447(9)$ while the sublattice magnetization $m_s = 0.30741(13)$ remains consistent with the $L_{\min} = 12$ value. Increasing to $L_{\min} = 16$ gives $m_1 = 0.5439(12)$, still too large, while the sublattice magnetization increases slightly to $m_s = 0.30742(16)$, which is fully compatible with the results of Refs. [8, 45] but with a larger error. The persistence of a discrepancy between m_1 from the fits and its predicted value can be taken as a indication of the pure polynomial not being the correct function to describe the $m_s^2(L)$ data.

Fitting with the predicted log correction included, the

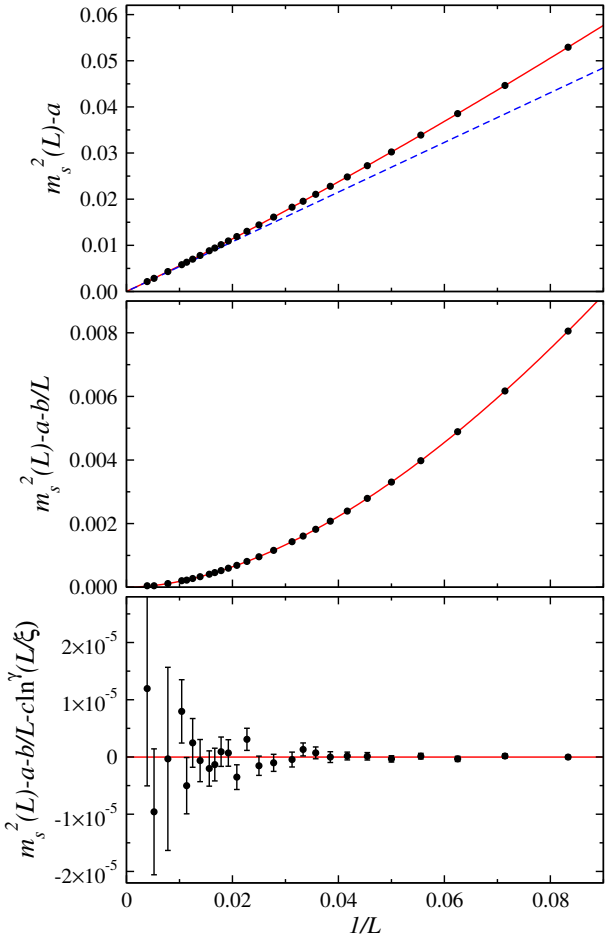


FIG. 5. The squared sublattice magnetization with the fitted terms of Eq. (17b) gradually removed from the data set and the corresponding remaining functions. No higher-order terms were included. In (a), only the constant $a = m_s^2(\infty)$ has been removed. The solid red curve shows the remaining part of the fitted function and the blue dashed line represents the term b/L , where the coefficient b is given by Eq. (17b) with the previously infinite-size extrapolated values of ρ_s and χ_\perp . In (b) also the linear term has been removed from both the data set and the fitted function. In (c) the remaining $\mu \ln^\gamma(L/\xi) L^{-2}$ term has been removed. There are no signs of higher-order corrections within the statistical errors.

values of ρ_s and χ_\perp in the linear coefficient Eq. (17b) are also fixed at their previously determined values, with their error bars taken into account by repeated fits with Gaussian noise. The constant m_s^2 and the linear coefficient are then constrained. In the log correction of the L^{-2} coefficient, the factor μ , the exponent γ , and the scale factor ξ are all unknown and used as free fitting parameters. Thus, there are four independent parameters and at this stage no higher-order polynomial terms (that might be expected) are included. For $L_{\min} = 8$, this fit is not statistically acceptable, the goodness-of-fit being $\chi^2/N_{\text{dof}} \approx 3$. For $L_{\min} = 10$, the quality of the fit is already reasonably good with $\chi^2/N_{\text{dof}} \approx 1.3$.

Recalling that the quality of the fourth-order polyno-

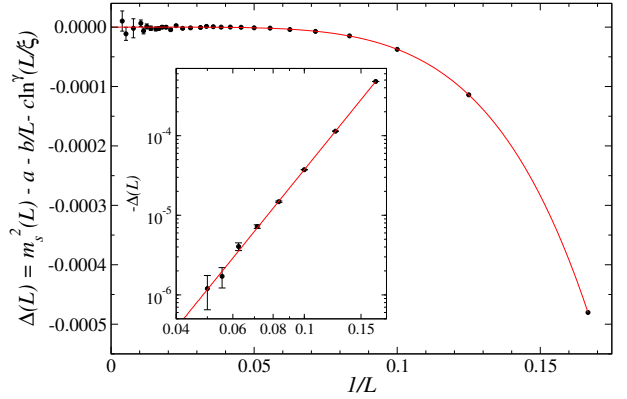


FIG. 6. Residual $\Delta(L)$ of the squared magnetization when all contributions from Eq. (17b) have been subtracted (in the corresponding expression on the y -axis, the fitting parameters are denoted a , b , ξ , and γ). This procedure leaves only the corrections, which in this fit is an L^{-5} term, shown as the red curve, added to Eq. (17b). The goodness-of-fit is $\chi^2/N_{\text{dof}} \approx 0.85$. The inset shows the same residuals (with a minus sign) in a log-log plot for the points that are clearly different from zero within error bars.

mial fit was poor for $L_{\min} = 10$, the fact that a good fit is now obtained without the L^{-3} and L^{-4} terms lends strong support to the presence of the multiplicative log correction, and, moreover, suggests that higher-order corrections must be very small. Excellent fits are obtained for $L_{\min} = 12$ and higher, with χ^2/N_{dof} in the range $0.7 \sim 0.8$ for $L_{\min} \in [12, 20]$. The order parameters obtained from the acceptable fits are remarkably stable for $L_{\min} \geq 12$, with $m_s = 0.307451(2)$ ($L_{\min} = 10$), $0.307444(3)$ ($L_{\min} = 12$), $0.307443(3)$ ($L_{\min} = 14$), $0.307443(3)$ ($L_{\min} = 16$), $0.307443(4)$ ($L_{\min} = 18$), and $0.307446(7)$ ($L_{\min} = 20$). The only slowly increasing error bar here reflects the fact that the log corrected L^{-2} term decays rather slowly and remains important also for the largest L_{\min} sizes considered here. Given the fast convergence, the $L_{\min} = 12$ result $m_s = 0.307444(3)$ is taken as the final result of this analysis. This result agrees perfectly with those of Refs. [8, 45], but with an error only a third of the previous size.

The value of the exponent γ on the log correction in Eq. (17b) was not predicted in Ref. [47]. In the $L_{\min} = 10$ fit, $\gamma = 0.73(1)$. For $L_{\min} = 12$ the exponent increases slightly but then remains very stable within its statistical error: $\gamma = 0.82(3)$ for $L_{\min} = 12$, $0.83(4)$ for $L_{\min} = 14$, $0.81(5)$ for $L_{\min} = 16$, $0.83(8)$ for $L_{\min} = 28$, and $0.70(14)$ for $L_{\min} = 20$. Considering the stability of the γ values for $L_{\min} \geq 12$, an error weighted average of the values can be taken as the final estimate; $\gamma = 0.82(4)$. The scale factor ξ in the log is also stable with respect to L_{\min} , with $\xi = 0.60(4)$ an overall representative result.

The good fit to $m_s^2(L)$ without higher-order corrections in Eq. (17b) is further illustrated in Fig. 5. The raw $L \geq 12$ data with the fitted constant m_s^2 subtracted off is shown in Fig. 5(a) along with the corresponding fit-

ted function (red curve). The contributions from only the linear term is also shown separately (dashed blue line). In Fig. 5(b) the linear term has also been subtracted, i.e., the function shown along with the data is only the quadratic term with its multiplicative log correction. Fig. 5(c) shows the SSE data with the full fitted function subtracted. The remaining values now fluctuate around zero in a way statistically consistent with Gaussian noise, as would also be expected because of the small χ^2/N_{dof} value quoted above. While some higher-order corrections to Eq. (17b) should of course exist, these results suggest that at least the L^{-3} correction should be extremely small or even completely absent.

Assuming that the higher-order corrections are pure integer powers of the inverse system size, a_n/L^n with $n \geq 3$, the smallest n for which the prefactor a_n is significant can be estimated by including the system sizes that were too small in the above fits using only the terms in Eq. (17b). When including all system sizes $L \geq 6$, a good fit cannot be obtained for $n = 3$. For $n = 4$ the fit is better, but still not statistically sound, with $\chi^2/N_{\text{dof}} \approx 4$. However, a very good fit with $\chi^2/N_{\text{dof}} \approx 0.85$ is produced when $n = 5$. The extrapolated sublattice magnetization in this case is $m_s = 0.307447(2)$, which is consistent with the results without the added correction but with a slightly smaller error. The exponent on the multiplicative log, $\gamma = 0.84(2)$, is likewise consistent with the previous result from the fit without L^{-5} correction, again with a reduced error. Thus, it appears that the L^{-5} term accounts well for the leading corrections to Eq. (17b). The other two parameters of the log term in the fit with this correction are $\xi = 0.56(1)$ and $\mu = 0.46(1)$.

The SSE data points after subtracting off the terms included in Eq. (17b) are shown in Fig. 6 along with the corresponding remaining part of the fitted function, i.e., the pure L^{-5} term. The correction has clearly visible impact for $L \lesssim 20$, though small changes in the other fitting parameter can account for the very small effects for $L \geq 12$, as demonstrated by the fact that the residuals are statistically zero in the fit without correction, Fig. 5(c). While the above analysis of the L^{-5} correction does not necessarily mean that L^{-3} and L^{-4} corrections are completely absent, they at least have to be very small relative to the L^{-5} term—possibly because of some cancellation effects. It is of course also possible that at least some of the higher-order terms also have log corrections.

D. Staggered susceptibility

The predicted form of the size-normalized staggered susceptibility $\chi_s(L)$ in Eq. (17c) is qualitatively different from the energy and the staggered magnetization in that also the constant term has a predicted form, depending on the above determined staggered magnetization in addition to the uniform susceptibility. Thus, the point here is not to determine the constant but to test its value against the predicted coefficient com-

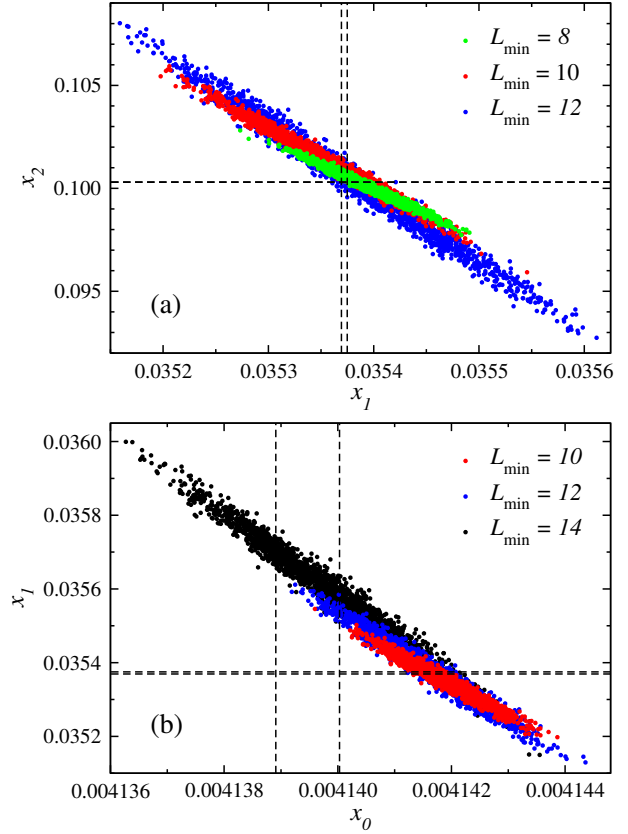


FIG. 7. (a) Scatter plot of the coefficients of the linear (x_1) and quadratic (x_2) corrections of the staggered susceptibility, based on 2000 fits with Gaussian noise added to the χ_s data in Table. I, with the minimum size $L_{\text{min}} = 8$ (green dots), 10 (red dots), and 12 (blue dots). The horizontal and vertical pairs of dashed lines (the horizontal lines almost coincide) indicate the expected values based on Eq. (17c) plus and minus two standard deviations, with ρ_s , c , and m_s^2 set to their previously determined values. (b) Similar plot of the constant term (x_0) and the coefficient of the linear correction (x_1) obtained with $L_{\text{min}} = 10$ (red), $L_{\text{min}} = 12$ (blue), and $L_{\text{min}} = 14$ (black).

puted from the $L \rightarrow \infty$ values of m_s^2 , χ_{\perp} , and c determined above. With three coefficients (x_0, x_1, x_2) , the distribution $P(x_0, x_1, x_2)$ from repeated fits is of interest. For easier visualization, the distribution will here be projected down to the two-dimensional distributions $P(x_0, x_1)$ and $P(x_1, x_2)$, based on sampling 2000 fits with Gaussian noise added to the $\chi_s(L)$ SSE data in Table I.

The linear and quadratic coefficients, x_1 and x_2 , are tested first in Fig. 7(a) with data points generated using fourth-order polynomial fits with $L_{\text{min}} = 8$, 10, and 12, all of which have $\chi^2/N_{\text{dof}} < 1$. Only marginally good consistency with the predicted window of coefficients is obtained with $L_{\text{min}} = 8$ and 10, but for $L_{\text{min}} = 12$ (and larger) the window is in a region of high probability density $P(x_1, x_2)$. However, the distribution $P(x_0, x_1)$ is far less convincing, as shown Fig. 7(b) for $L_{\text{min}} = 10$, 12, and 14. While the individual x_0 and x_1 windows do have large overlaps with the distribution, the joint (x_0, x_1) window

is far away from the high-probability region, to the extent that an agreement is statistically very unlikely (noting also that the indicated window corresponds to two standard deviations of the mean coefficients). The trend with increasing L_{\min} is also not indicative of eventual agreement for $L_{\min} > 14$ (until the size of the distribution grows too large for meaningful comparisons).

As discussed in Sec. II C, there may still be some $T > 0$ contributions left in $\chi_s(L = 96)$ at $\beta/L = 64$, leading to underestimation of the value by 1–2 of its error bars in Table I. To exclude $T > 0$ effects as the cause of the mismatch in Fig. 7(b), fits with one or several large systems excluded were also carried out. In all cases the changes in the distributions are very minor and the allowed window falls within the distribution only when the fluctuations become too large to produce meaningful results (when many small and large sizes have been removed).

The behavior here is similar to the case of m_s^2 fitted to a polynomial in L^{-1} without the log correction in Sec. III C, where the linear coefficient m_1 was not consistent with the predicted form in Eq. (17b). The discrepancy was only resolved by including the log correction to the quadratic term. Given that m_s^2 and χ_s are strongly related to each other in terms of their definitions (being space and space-time integrals, respectively, of the spin correlation function), one might suspect that also χ_s should have a log correction, perhaps in the cubic term. The fitted polynomial may then skew the coefficients of the lower-order term in a similar way as in the case of m_1 in the m_s^2 fits.

In principle, another potential reason for the discrepancies could be that some of the extrapolated coefficients in Eq. (17b) have errors beyond the quoted statistical errors. The most likely candidate for such errors would be in $x_0 = (2/3)m_s^2\chi_{\perp}$, which would fix the problem in Fig. 7(b) if the window is shifted by $x_0 \rightarrow ax_0$ with the factor $a \approx 1.0005$. Such a shift would imply the presence of substantial extrapolation errors in either χ_{\perp} or m_s^2 , or both. In particular, a shift of only m_s^2 , which is a factor in all the coefficients x_0, x_1, x_2 in Eq. (17b) would solve the problem in Fig. 7(b) and also leave Fig. 7(a) in consistency. Such a large extrapolation error in m_s is unlikely, however, as the value would have to increase to $m_s \approx 0.30752$, which is very far out of the range determined in Sec. III C and is also about 10 error bars away from the best previous estimates [8, 45]. The remaining possibility of a shift in χ_{\perp} is also unlikely, based on many different extrapolations performed that deliver results consistent with that reported in Sec. III A. Thus, the presence of a logarithmic correction in Eq. (17c), whether in one of the terms displayed or in some higher-order correction, remains the most likely explanation for the discrepancy in Fig. 7(b).

Given that the pure polynomial fitting functions may not be strictly correct, to report an independent (of the previously determined coefficients) value of the constant χ_s/L^2 in the $L \rightarrow \infty$ limit, results including the smallest system sizes should be regarded with some suspicion.

even though the χ^2/N_{dof} values are good. The effects of these unknown corrections should diminish with increasing L_{\min} . Given that the $L_{\min} = 14$ distribution of x_0 from Fig. 7(b) overlaps well with the predicted window, the corresponding mean value here is taken as a reliable result; $\chi_s/L^2 = 0.04140(1)$. The value based on $m_1 = (2/3)m_s^2\chi_{\perp}$ (assuming that this indeed equals χ_s) is still of higher statistical precision, however, at 0.041384(4).

IV. OPEN AND CYLINDRICAL BOUNDARY CONDITIONS

Some of the often used lattice many-body methods are not efficient for 2D systems with periodic boundary conditions, e.g., cylindrical boundaries are typically used in DMRG and related matrix-product state methods [13, 14, 53] while some of the TN-based methods are only practically applicable with fully open boundaries [15, 16]. With cylindrical boundaries, it is further advantageous to use non-square lattices of size $L_x \times L_y$ with L_y larger than the size L_x in the periodic direction. In some cases the limit $L_y/L_x \rightarrow \infty$ can be taken, in which case the system strictly is one-dimensional, but the 2D limit can in principle (though often not in practice) be studied for increasing L_x to realize the 2D limit. In other cases it is better to keep the aspect ratio fixed, e.g., with $L_y/L_x = 2$. Here some results for open $L \times L$ systems and cylindrical $L \times 2L$ systems at $\beta/L = 32$ will be presented, but for a more limited set of quantities and at lower statistical precision than for the periodic boundary conditions in the preceding sections. The ground state energy will now be given per interacting bond N_b , while the squared sublattice magnetization and the staggered susceptibility will be normalized by the system volume N as before. Results are listed in Tables II and III. For the largest systems, the staggered susceptibility was not computed as much larger β/L values would be needed for convergence. The energy and sublattice magnetization are $T \rightarrow 0$ converged.

The lack of L^{-1} and L^{-2} terms in the dependence on the energy on the system size in Eq. (17b) should only be expected with periodic conditions. With one or both boundaries open, an L^{-1} term should be expected, and there is also no reason for the L^{-2} term to be absent. Indeed, the E_0/N_b data can only be fitted if both these terms are included. Fits are shown in Fig. 8 for all boundary conditions. For the periodic case, the fit is the one discussed in Sec. III B and its extrapolated energy was used to constrain the fits for the other two boundary conditions. There are no predictions for the finite-size corrections for non-periodic systems and the purpose of the fits here is only to demonstrate the L^{-1} and L^{-2} corrections and the expected consistency of the infinite-size energies computed with different boundary conditions.

With fully open boundaries, the convergence of the sublattice magnetization to the previously determined

TABLE II. SSE data for $L \times L$ systems with open boundary conditions. The ground state energy is normalized by the number of interaction bonds $N_b = 2(L^2 - L)$.

L	E_0/N_b	m_s^2	χ_s/L^2
6	0.3621133(1)	0.164510(1)	0.0098278(2)
8	0.3537355(1)	0.135629(2)	0.0070608(2)
10	0.3492534(1)	0.120522(2)	0.0058259(2)
12	0.3464731(1)	0.111577(2)	0.0051646(2)
14	0.3445836(1)	0.105834(2)	0.0047687(3)
16	0.3432169(1)	0.101926(3)	0.0045128(3)
18	0.3421827(2)	0.099160(4)	0.0043392(5)
20	0.3413732(2)	0.097131(4)	0.0042171(5)
22	0.3407218(2)	0.095619(5)	0.0041250(6)
24	0.3401870(2)	0.094454(5)	0.0040592(6)
26	0.3397397(2)	0.093538(6)	0.0040081(6)
28	0.3393603(2)	0.092827(4)	0.0039687(8)
32	0.3387504(2)	0.091825(7)	—
48	0.3373629(2)	0.09022(2)	—
64	0.3366865(2)	0.08998(2)	—
96	0.33602096(8)	0.09031(3)	—
128	0.33569204(9)	0.09076(5)	—

TABLE III. SSE data for $L \times 2L$ lattices with cylindrical boundary conditions (periodic in the shorter direction and open in the longer direction). The ground state energy is normalized by the number of interaction bonds $N_b = 2L^2 - L$.

L	E_0/N_b	m_s^2	χ_s/L^2
4	0.3532363(2)	0.170293(2)	0.0083710(2)
6	0.3427879(2)	0.140311(3)	0.0066647(3)
8	0.3397983(2)	0.125772(3)	0.0058507(3)
10	0.3384370(2)	0.117465(3)	0.0053900(4)
12	0.3376621(2)	0.112218(4)	0.0051033(6)
14	0.3371612(2)	0.108676(5)	0.0049103(6)
16	0.3368096(2)	0.106134(7)	0.0047720(9)
18	0.3365491(2)	0.104248(6)	0.0046701(8)
20	0.3363476(2)	0.102801(8)	0.0045925(9)
24	0.3360555(3)	0.10073(2)	—
32	0.3357061(3)	0.09843(3)	—
48	0.3353698(3)	0.09638(5)	—
64	0.3352053(2)	0.09558(6)	—

value is not obvious from the results in Table II. With increasing L , $m_s^2(L)$ drops below the expected $L \rightarrow \infty$ value and the results for the two largest system sizes showing the onset of a nonmonotonic behavior before the necessary ultimate convergence to the same value $m_s^2 \approx 0.09445$ as for the periodic systems. The staggered susceptibility as well drops significantly below the results for the periodic systems and nonmonotonic behavior will likely set in here as well, for system sizes larger

than those available. The results for cylindrical systems in Table III do not indicate any nonmonotonicity and the results can be extrapolated to values consistent with the periodic lattices.

Suppression of the staggered magnetization close to open boundaries should be expected and the results for m_s^2 in Tables II and III suggest that the effects are much more dramatic in the case of fully open boundaries. Large fluctuations close to the corners can likely explain the differences. To more quantitatively investigate the boundary effects on the order parameter, the squared sublattice magnetization can be broken up into site dependent contributions. Using the normalized sublattice magnetization m_s^z in Eq. (4), a location dependent squared order parameter can be defined;

$$m_s^2(\mathbf{r}) = 3\langle S^z(\mathbf{r})m_s^z \rangle (-1)^{r_x+r_y}, \quad (20)$$

so that the full (averaged) value is $m_s^2 = \sum_{\mathbf{r}} m_s^2(\mathbf{r})/N$. A relative distortion field can further be defined as

$$D(d_x, d_y) = 1 - \frac{m_s^2(\mathbf{r}_d)}{m_s^2(\mathbf{r}_{\text{center}})}, \quad (21)$$

where $\mathbf{d} = (d_x, d_y)$ is the distance to the site at \mathbf{r}_d relative to a reference point on an edge. The normalization is by the squared order parameter at a site $\mathbf{r}_{\text{center}}$ closest to the center of the system (in practice averaged over all such equivalent sites), where the suppression (distortion) of the order parameter is the smallest. By definition $d(\mathbf{r}_{\text{center}}) = 0$ at the central sites. $D(d_x, d_y)$ should strictly correspond to the true distortion field only as $L \rightarrow \infty$, where the order parameter at $\mathbf{r}_{\text{center}}$ will truly take its bulk value without finite-size effects. The vanishing of $D(\mathbf{r}_{\text{center}})$ for any L is just a finite-size aspect along with the overall size dependence of the sublattice magnetization, which is partially compensated for here by using ratios of local order parameters in Eq. (21). For the open $L \times L$ lattices with even L there are four equivalent central locations $\mathbf{r}_{\text{center}}$ while in the cylindrical $L \times 2L$ systems there are $2L$ such sites (two central “rings” of length L).

In principle it is possible to compute the distortion using linear spinwave theory (which has been applied to a related open-boundary problem [54]) or some more sophisticated approach, but this is beyond the scope of the present work. By testing different functional forms, it was found that a stretched exponential describes the data very well. With d denoting the distance from an open edge or corner along a line on the lattice (to be defined more precisely below), the distortion as defined in Eq. (21) can be well described by the form

$$D(d) \propto \left[\exp(-\sqrt{d/\xi}) + \exp\left(-\sqrt{(L-1-d)/\xi}\right) - \exp\left(-\sqrt{(L/2-1)/\xi}\right) - \exp\left(\sqrt{L/2\xi}\right) \right], \quad (22)$$

where $L = L_y$ for the fully open lattices and $L = L_y/2$ for the cylindrical systems. The first term is the distortion from the edge (or corner) with respect to which the

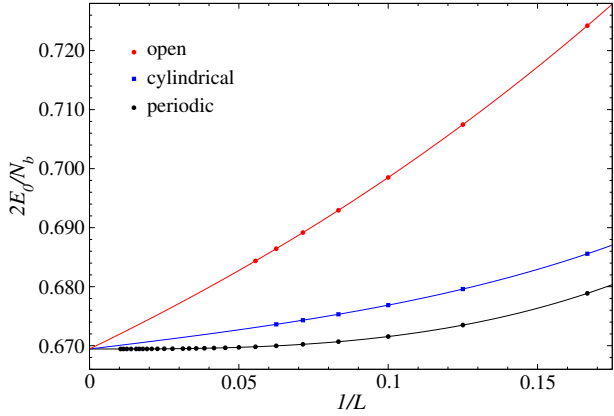


FIG. 8. Twice the ground state energy per bond for systems with different boundary conditions; periodic $L \times L$ (black circles), cylindrical $L \times 2L$ (blue squares), and open $L \times L$ (red circles). The curves are polynomial fits, without L^{-1} and L^{-2} terms for the periodic systems but including those for the other cases.

distance d is measured and the second term reflects the opposite edge (or corner) at distance $L - 1 - r$ (with the distance between the two edges being $L - 1$ and the $\sqrt{2}$ factor in a corner-corner diagonal direction is absorbed into ξ). The last two terms ensure the imposed condition $d(r) = 0$ in Eq. (21) for the center sites located at $d = L/2 - 1$ and $d = L/2$. For large L and distances $d \ll L$, only the first term contributes significantly but the other terms are important for the rather small system sizes and distances considered here.

Results are shown in Fig. 9 for all three boundary conditions. In the case of the fully open $L \times L$ lattices (with L an even number), the distance in Fig. 9(a) is defined from one of the two sites closest to the mid-point of an edge, extending toward the center of the system along the line perpendicular to the edge in question. In Fig. 9(b), the distance is measured from one of the corners of the open lattice along the corresponding diagonal direction, not taking into account the factor $\sqrt{2}$ from the length of the diagonal of a plaquette of unit length. Fig. 9(c) is for the cylindrical system of size $L \times 2L$, with d being the distance from a site on the edge along a line in the longer direction. In all cases Eq. (22) describes the behavior well for sufficiently large d . The short-distance deviations from the form are, perhaps surprisingly, much larger for the cylindrical lattices. In all cases there are still finite size effects in the decay constant ξ , but the trend for increasing system size indicates convergence, with the value for the largest system already close to converged. For the largest systems, $\xi \approx 1.2$ in Fig. 9(a), $\xi \approx 1.3$ in Fig. 9(b), and $\xi \approx 2.5$ in Fig. 9(c). The largest distortion, exactly on the edge, is $D(0) \approx 0.22$ in both Fig. 9(a) and Fig. 9(c), while in the case of the corner in Fig. 9(b) it is about twice as large; $D(0) \approx 0.45$.

Even though the (stretched) exponential decay guarantees that the spatially averaged m_s^2 when $L \rightarrow \infty$ will

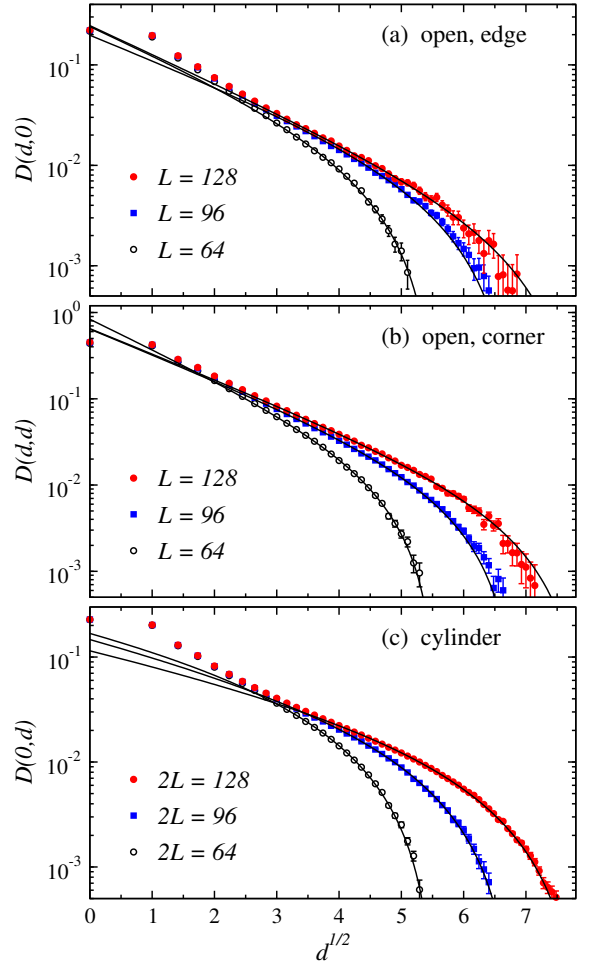


FIG. 9. Distortion field of the order parameter, Eq. (21), vs the square-root of the distance from an edge. In (a), d is the distance along a line $(d, 0)$ extending from a site closest to the mid-point of the edge of an open $L \times L$ lattice toward the center of the system, while in (b) the line extends from a corner in the diagonal direction (d, d) . In (c), the distance is from a site on the open edge of length L of an $L \times 2L$ cylinder along the line $(0, d)$ perpendicular to the open edge. The curves show fits to the stretched exponential decay, Eq. (22).

be the same for all three boundary conditions, the distortion is still relatively large for the moderate lattice sizes considered here, especially because of the corners in the case of the fully open boundaries. The nonmonotonic behavior seen for the largest system sizes in Table II is then explained as arising from the large boundary reduction of the order parameter, which affects the spatially averaged value up to large system sizes. The boundary effect also asymptotically implies a finite-size correction of the form L^{-1} in the average, which can be larger than the linear coefficients in the periodic systems in Eq. (17b). This appears to be the case for the open boundaries and the asymptotic approach to the infinite-size value is then from below, in contrast to the approach from above in the case of the periodic systems.

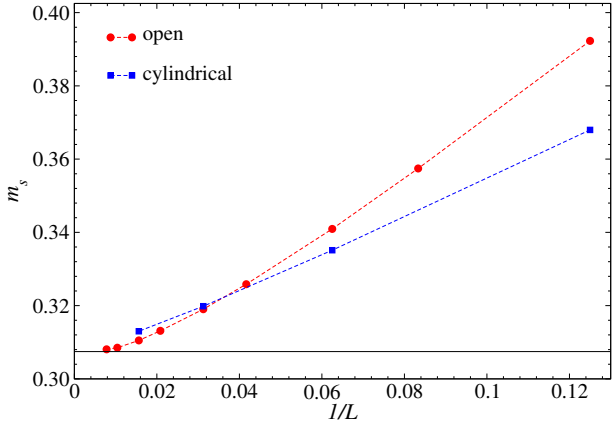


FIG. 10. Inverse-size dependence of the sublattice magnetization at the sites closest to the center of systems with open (red circles) and cylindrical (blue squares) boundary conditions. The horizontal line shows the $L \rightarrow \infty$ value obtained in Sec. III C for systems with periodic boundaries.

It is also useful to examine the local staggered magnetization $m_s(\mathbf{r})$ with \mathbf{r} at the center of the system (averaged over all the symmetrically equivalent sites closest to the center). Results are shown for both open and cylindrical systems in Fig. 10. Here the results for the cylindrical systems are fully consistent with an approach from above to the expected infinite-size value. Extrapolations are not shown here as the exact $L \rightarrow \infty$ value is sensitive to the functional form used and it is not clear whether the logarithmic contribution in Eq. (17b) survives for the cylindrical systems. For the open systems, the results in Fig. 10 flatten out for the largest system sizes and a naive extrapolation with a polynomial gives an extrapolated order parameter below the expected value. Most likely, the behavior here is again nonmonotonic, arising from the open boundaries significantly affecting also the spins in the center of the system.

V. DISCUSSION

The Néel ordered ground state of 2D Heisenberg $S = 1/2$ antiferromagnet represents a corner stone in the field of quantum magnetism. Beyond specific applications to quantum magnetism, the mechanism of $SO(3)$ spin-rotational symmetry breaking is universal and deserving of detailed quantitative understanding. A primary motivation for this work was to obtain unbiased high-precision results for the key ground state parameters of the model, which beyond very small system sizes is possible only with statistically exact QMC algorithms, such as the SSE method used here. A previously often cited list of ground state parameters up to system size $L = 16$ [44] is now outdated, considering that some of the emerging many-body methods are now exceeding the statistical precision reported there, at least in the case of the ground state energy for L up to 10 [22]. The trend of increas-

ingly good variational states based on TNs and NNs will only continue and better benchmarks are called for. The raw data listed here in Tables I (for periodic lattices), II (open lattices), and III (cylindrical lattices) are of much higher precision than previously and also cover a broader range of physical observables—including quantities, such as the staggered susceptibility, that are more challenging to compute with TN and NN approaches than the energy and the order parameter.

The results for the $L \rightarrow \infty$ extrapolated ground state parameters are also likely the most precise to date. For ease of reference, the best estimates of all the quantities considered are repeated here:

$$e = -0.669441857(7), \quad (23a)$$

$$\rho_s = 0.180752(6), \quad (23b)$$

$$\chi_{\perp} = 0.065690(5), \quad (23c)$$

$$c = 1.65880(6), \quad (23d)$$

$$m_s = 0.307447(2), \quad (23e)$$

$$\chi_s/L^2 = 0.004140(1). \quad (23f)$$

The largest improvement with respect to previous works is in the energy, where the error bar is almost three orders of magnitude smaller than in Ref. [44]. This improvement in precision is not surprising, considering the growth of computing power over almost 30 years in combination with the improvements in the SSE algorithm, in particular the introduction of loop updates [4, 7]. The algorithmic improvements are more important for some of the other quantities, however, since the SSE energy estimator is rotationally invariant and not sensitive to the slowest mode of the stochastic evolution of the SSE configurations (even with inefficient local updates [44]), which physically correspond to long-wavelength fluctuations of the order parameter and its overall rotation in spin space [44].

In recent work with recurrent NNs, ground state energies for $L \leq 32$ were extrapolated to $e_0 = -0.6694886(5)$ in the thermodynamic limit [27]. This value differs from the present result above by almost 100 of its error bars, likely primarily because of the non-variational errors introduced by extrapolating the finite-size results to zero sampling variance. Though the result is only good to the fourth decimal place, the current activities in pushing NNs to unprecedented precision nevertheless illustrates the increasing needs for reliable benchmarks, such as the extrapolated results above and the raw finite-size data listed in tables in the preceding sections.

A second purpose of this work, beyond determining the ground state parameters to unprecedented precision, was to test finite-size corrections predicted by chiral perturbation theory [28, 29, 47], which with the improved data was accomplished at a level far exceeding previous works. A multifaceted statistical analysis showed complete agreement with leading and subleading corrections to both the energy and the sublattice magnetization. In the latter case, the first subleading (L^{-2}) correction is modified by a multiplicative \log [29], $\ln^{\gamma}(L)$, the presence of which

was confirmed. The previously unknown value of the exponent $\gamma = 0.82(4)$ was determined. The corrections to the related staggered susceptibility also show evidence of a log correction in higher-order terms, as evidenced from minor discrepancies between coefficients from polynomial fits and their predicted forms in terms of other ground state parameters. This result should serve as a motivation to extend the chiral perturbation theory to higher order—clearly not an easy task, considering the already very sophisticated calculations underlying the existing predictions in Eqs. (17).

With open and cylindrical boundary conditions, the reduction of the order parameter at the open edges was found to follow a stretched exponential form asymptotically. For large sufficiently systems, the order parameter at distance r from an edge takes the form $m_s(r) = m_s(\infty) - A \exp(-\sqrt{r/\xi})$, with the parameters A and ξ depending on the reference point on the boundary (specifically, its distance from corners). In the Heisenberg model the maximum distortion A is rather large, up to almost half of $m_s(\infty)$, and ξ of order one. The overall edge effects therefore significantly reduce the order parameter integrated over the entire system, in some cases even leading to nonmonotonic finite-size behavior. These effects should be kept in mind when working with non-periodic boundaries, as data for a range of small system sizes can give misleading results—this will be the case

also if only a central region of the system is used, if the size of that region grows with L . Even if only the most central spins are used, the edge effects can still be important; likely even more so in systems with weaker Néel order than the standard Heisenberg model studied here.

As an example of the computational effort involved to generate the data presented here, in the case of the $L = 96$ system at inverse temperature $\beta = 64L$, one full SSE updating sweep with measurements of observables required about 10s using Intel Xeon Gold 6000-series CPUs. Approximately 1.5×10^8 such steps were performed, for a total of about 4×10^5 hours of CPU core time, distributed over a large number of CPU cores. In the case of $L = 8$ at $\beta = 32L$, an updating sweep takes about 10^{-3} s and about 2×10^{11} steps were carried out for a total of about 5×10^4 core hours (and this accounted for about half of the statistics for this system size, the remainder coming from $\beta = 64L$ runs).

ACKNOWLEDGMENTS

The author would like to thank Uwe-Jens Wiese for discussions. This work was supported by the Simons Foundation under Grant No. 511064. The numerical calculations were carried out on the Shared Computing Cluster managed by Boston University's Research Computing Services.

[1] E. Y. Loh, Jr., J. E. Gubernatis, R. T. Scalettar, S. R. White, D. J. Scalapino, and R. L. Sugar, Sign problem in the numerical simulation of many-electron systems, *Phys. Rev. B* **41**, 9301 (1990).

[2] P. Henelius and A. W. Sandvik, Sign problem in Monte Carlo simulations of frustrated quantum spin systems, *Phys. Rev. B* **62**, 1102 (2000).

[3] M. Troyer and U.-J. Wiese, Computational Complexity and Fundamental Limitations to Fermionic Quantum Monte Carlo Simulations, *Phys. Rev. Lett.* **94**, 170201 (2005).

[4] A. W. Sandvik, Stochastic series expansion method with operator-loop update, *Phys. Rev. B* **59**, R14157 (1999).

[5] O. F. Syljuåsen and A. W. Sandvik, Quantum Monte Carlo with directed loops, *Phys. Rev. E* **66**, 046701 (2002).

[6] A. W. Sandvik, Computational Studies of Quantum Spin Systems, *AIP Conf. Proc.* **1297**, 135 (2010).

[7] H. G. Evertz, G. Lana, and M. Marcu, Cluster algorithm for vertex models, *Phys. Rev. Lett.* **70**, 875 (1993).

[8] A. W. Sandvik and H. G. Evertz, Loop updates for variational and projector quantum Monte Carlo simulations in the valence-bond basis, *Phys. Rev. B* **98**, 024407 (2010).

[9] N. Ma, P. Weinberg, H. Shao, W. Guo, D.-X. Yao, and A. W. Sandvik, Anomalous Quantum-Critical Scaling Corrections in Two-Dimensional Antiferromagnets, *Phys. Rev. Lett.* **121**, 117202 (2018).

[10] A. W. Sandvik and B. Zhao, Consistent Scaling Exponents at the Deconfined Quantum-Critical Point, *Chin. Phys. Lett.* **37**, 057502 (2020).

[11] J. Takahashi, H. Shao, B. Zhao, W. Guo, A. W. Sandvik, SO(5) multicriticality in two-dimensional quantum magnets, *arXiv:2405.06607*.

[12] S. R. White, Density-matrix algorithms for quantum renormalization groups, *Phys. Rev. B* **48**, 10345 (1993).

[13] U. Schollwoeck, The density-matrix renormalization group in the age of matrix product states, *Ann. Phys.* **326**, 96 (2011).

[14] E. M. Stoudenmire and S. R. White, Real-space parallel density matrix renormalization group, *Phys. Rev. B* **87**, 155137 (2013).

[15] V. Murg, F. Verstraete, and J. I. Cirac, Exploring frustrated spin systems using projected entangled pair states, *Phys. Rev. B* **79**, 195119 (2009).

[16] W.-Y. Liu, S. Dong, C. Wang, Y. Han, H. An, G.-C. Guo, and L. He, Gapless spin liquid ground state of the spin-1/2 J_1 - J_2 Heisenberg model on square lattices, *Phys. Rev. B* **98**, 241109 (2018).

[17] R. Orús, Tensor networks for complex quantum systems, *Nat. Rev. Phys.* **1**, 538 (2019).

[18] P. Corboz, Y. Zhang, B. Ponsioen, and F. Mila, Quantum spin liquid phase in the Shastry-Sutherland model revealed by high-precision infinite projected entangled-pair states, *arXiv:2502.14091*.

[19] G. Carleo and M. Troyer, Solving the quantum many-body problem with artificial neural networks, *Science* **355**, 602 (2017).

[20] H. Lange, A. Van de Walle, A. Abedinnia, and A. Bohrdt, *arXiv:2502.14091*.

From Architectures to Applications: A Review of Neural Quantum States, *Quantum Sci. Technol.* **9**, 040501 (2024).

[21] D. Wu, R. Rossi, F. Vicentini, and G. Carleo, From tensor-network quantum states to tensorial recurrent neural networks, *Phys. Rev. Res.* **5**, L032001 (2023).

[22] A. Chen and M. Heyl, Empowering deep neural quantum states through efficient optimization, *Nat. Phys.* **20**, 1476 (2024).

[23] R. Rende, S. Goldt, F. Becca, and L. L. Viteritti, Fine-tuning neural network quantum states, *Phys. Rev. Res.* **6** 043280 (2024).

[24] M. Bortone, Y. Rath, and G. H. Booth, Impact of conditional modelling for a universal autoregressive quantum state, *Quantum* **8**, 1245 (2024).

[25] J. Wang, J. Surace, I. Frérot, B. Legat, M.-O. Renou, V. Magron, and Acín, Certifying Ground-State Properties of Many-Body Systems, *Phys. Rev. X* **14** 031006 (2024).

[26] I. Kull, N. Schuch, B. Dáv, and M. Navascués, Lower Bounds on Ground-State Energies of Local Hamiltonians through the Renormalization Group, *Phys. Rev. X* **14**, 021008 (2024).

[27] M. S. Moss, R. Wiersema, M. Hibat-Allah, J. Carrasquilla, and R. G. Melko, Leveraging recurrence in neural network wavefunctions for large-scale simulations of Heisenberg antiferromagnets: the square lattice, arXiv:2502.17144.

[28] P. Hasenfratz and F. Niedermayer, Finite size and temperature effects in the AF Heisenberg model, *Z. Phys. B* **92**, 91 (1993).

[29] F. Niedermayer and C. Weiermann, The rotator spectrum in the delta-regime of the O(n) effective field theory in 3 and 4 dimensions, *Nucl. Phys. B* **842**, 248 (2011).

[30] P. W. Anderson, New Approach to the Theory of Superexchange Interactions, *Phys. Rev.* **115**, 2 (1959).

[31] B. I. Halperin and P. C. Hohenberg, Hydrodynamic Theory of Spin Waves, *Phys. Rev.* **188**, 898 (1969).

[32] J. Oitmaa and D. D. Betts, Ground state properties of the Heisenberg antiferromagnet and XY magnet in three dimensions, *Phys. Lett. A* **68**, 450 (1978).

[33] J. Oitmaa and D. D. Betts, The ground state of two quantum models of magnetism, *Can. J. Phys.* **56**, 897 (1978).

[34] D. A. Huse, Ground-state staggered magnetization of two-dimensional quantum Heisenberg antiferromagnets, *Phys. Rev. B* **37**, 2380 (1988).

[35] J. D. Reger and A. P. Young, Monte Carlo simulations of the spin-1/2 Heisenberg antiferromagnet on a square lattice, *Phys. Rev. B* **37**, 5978 (1988).

[36] S. Chakravarty, B. I. Halperin, and D. R. Nelson, Two-dimensional quantum Heisenberg antiferromagnet at low temperatures, *Phys. Rev. B* **39**, 2344 (1989).

[37] S. Liang, Existence of Néel order at T=0 in the spin-1/2 antiferromagnetic Heisenberg model on a square lattice, *Phys. Rev. B* **42**, 6555 (1990).

[38] M. S. Makivic and H.-Q. Ding, Two-dimensional spin-1/2 Heisenberg antiferromagnet: A quantum Monte Carlo study, *Phys. Rev. B* **43**, 3562 (1991).

[39] E. Manousakis, The spin-1/2 Heisenberg antiferromagnet on a square lattice and its application to the cuprous oxides, *Rev. Mod. Phys.* **63**, 1 (1991).

[40] K. J. Runge, Quantum Monte Carlo calculation of the long-range order in the Heisenberg antiferromagnet, *Phys. Rev. B* **45**, 7229 (1992).

[41] K. J. Runge, Finite-size study of the ground-state energy, susceptibility, and spin-wave velocity for the Heisenberg antiferromagnet, *Phys. Rev. B* **45**, 12292 (1992).

[42] U.-J. Wiese and H.-P. Ying, A determination of the low energy parameters of the 2-d Heisenberg antiferromagnet, *Z. Phys. B* **93**, 147 (1994).

[43] B. B. Beard and U.-J. Wiese, Simulations of Discrete Quantum Systems in Continuous Euclidean Time *Phys. Rev. Lett.* **77**, 5130 (1996).

[44] A. W. Sandvik, Finite-size scaling of the ground-state parameters of the two-dimensional Heisenberg model, *Phys. Rev. B* **56**, 11678 (1997).

[45] F.-J. Jiang and U.-J. Wiese, High-precision determination of low-energy effective parameters for a two-dimensional Heisenberg quantum antiferromagnet *Phys. Rev. B* **83**, 155120 (2011).

[46] A. Sen, H. Suwa, and A. W. Sandvik, Velocity of excitations in ordered, disordered, and critical antiferromagnets, *Phys. Rev. B* **92**, 195145 (2015).

[47] H. Neuberger and T. Ziman, Finite-size effects in Heisenberg antiferromagnets, *Phys. Rev. B* **39**, 2608 (1989).

[48] D. S. Fisher, Universality, low-temperature properties, and finite-size scaling in quantum antiferromagnets, *Phys. Rev. B* **39**, 11783 (1989).

[49] A. W. Sandvik and J. Kurkijärvi, Quantum Monte Carlo simulation method for spin systems, *Phys. Rev. B* **43**, 5950 (1991).

[50] E. L. Pollock and D. M. Ceperley, Path-integral computation of superfluid densities, *Phys. Rev. B* **36**, 8343 (1987).

[51] C. Lavalle, S. Sorella, and A. Parola, Anomalous Finite Size Spectrum in the S=1/2 Two Dimensional Heisenberg Model, *Phys. Rev. Lett.* **80**, 1746 (1998).

[52] F. Niedermayer and P. Weisz, Casimir squared correction to the standard rotator Hamiltonian for the O(n) sigma-model in the delta-regime, *J. High Energy Phys.* **2018**, 70 (2018).

[53] J. Yang, A. W. Sandvik, and L. Wang, Quantum criticality and spin liquid phase in the Shastry-Sutherland model, *Phys. Rev.* **105**, L060409 (2022).

[54] S. Sanyal, A. Banerjee, K. Damle, and A. W. Sandvik, Antiferromagnetic order in systems with doublet $S_{\text{tot}} = 1/2$ ground states, *Phys. Rev.* **86**, 064418 (2012).